Whirl flutter analysis of prop-rotors using unsteady aerodynamics reduced-order models

M. Gennaretti
Department of Mechanical and Industrial Engineering
University Roma Tre, Rome, Italy

L. Greco
INSEAN, Italian Ship Model Basin
Rome, Italy

ABSTRACT

The prediction of this aeroelastic phenomenon is an urgent need of the designer and requires devoted numerical tools. This work examines the influence of the accuracy of the aerodynamic modelling on whirl flutter analysis, with particular attention to those models that can conveniently be applied to preliminary design and control purposes. Considering a simple pylon/prop-rotor structure, the aeroelastic instability boundaries are identified by 2D quasi-steady and 2D unsteady aerodynamics theories, along with a 3D unsteady, potential flow BEM solver. A methodology for deriving reduced-order models from unsteady aerodynamic solutions is used. The numerical investigation highlights that the accuracy of the aerodynamic solver included in the analysis may be of crucial importance. The use of 2D aerodynamic models does not always guarantee conservative stability predictions, and this is particularly true for three-bladed rotors where a fully 3D unsteady solver coupled with a wake alignment algorithm seems to be necessary.

NOMENCLATURE

a	lift curve slope
$\mathbf{A}_0$, $\mathbf{A}_1$	transfer function matrices between pylon dofs and blade aerodynamic loads
$\mathbf{A}$, $\mathbf{B}$, $\mathbf{C}$	matrices related to the rational matrix approximation
c	section chord
c_D	section drag coefficient
$C(k)$	Theodorsen lift deficiency function
$\bar{C}_x, \bar{C}_y$	non-dimensional yaw and pitch damping
$\boldsymbol{E}_n(s)$	transcendental transfer function matrix between $\mathbf{v}$ and blade aerodynamic loads
f^{in}, f^{out}	in-plane and out-of-plane aerodynamic section loads
$\bar{F}_n$	in-plane aerodynamic non-dimensional force on the n-th blade
h	pivot point distance from rotor hub
I_b	blade moment of inertia wrt the hub
$\bar{I}_x$, $\bar{I}_y$	non-dimensional pylon yaw and pitch moments of inertia (including rotor mass)
$\mathbf{K}$	non-dimensional pylon spring restraints matrix
$k = \omega c/2\Omega r$	section reduced frequency
$\bar{K}_x$, $\bar{K}_y$	non-dimensional spring restraints of pylon motion about the pivot
L, D	lift and drag force
$\mathbf{M}$, $\mathbf{C}$	non-dimensional pylon mass and damping matrices (including rotor inertia)
$M_{¼}$	torque moment about the ¼-chord point
$\mathbf{m}_{aer}$	non-dimensional rotor aerodynamic moments on the pivot
$\bar{M}_n^f$, $\bar{M}_n^t$	non-dimensional flap and torsion aerodynamic moments wrt hub on the n-th blade
N	number of rotor blades
N_a	number of poles included in the rational matrix approximation
r	blade radial station
$\boldsymbol{r}$	additional aerodynamic states vector

Paper No. 3226. Manuscript received 4 August 2007, revised 11 January 2008, accepted 29 February 2008.

https://doi.org/10.1017/S0001924000002207 Published online by Cambridge University Press

R	rotor radius
s	complex reduced frequency
u_T	in-plane blade section velocity with respect to fluid at ¾-chord point
u_P	out-of-plane blade section velocity with respect to fluid at ¾-chord point
V	axial velocity
$\boldsymbol{\nu} = \{v_1, v_2, v_3, \omega_1, \omega_2, \omega_3\}^T$	rotating-frame velocity components of the rotor rigid-body motion
v_i	velocity induced by the prop-rotor wake
$\boldsymbol{\alpha} = \{\alpha_y\ \alpha_x\}^T$	pylon yaw and pitch degrees of freedom
ε	angular velocity of the blade section in the rotating frame
γ	Lock number
ϑ	blade section pitch angle
$\lambda = R/c$	blade aspect ratio
$\mu = V/\Omega R$	advance ratio
ρ	air density
φ	inflow angle
ϕ	velocity potential function
ψ	rotor azimuth position
Ω	rotor angular velocity

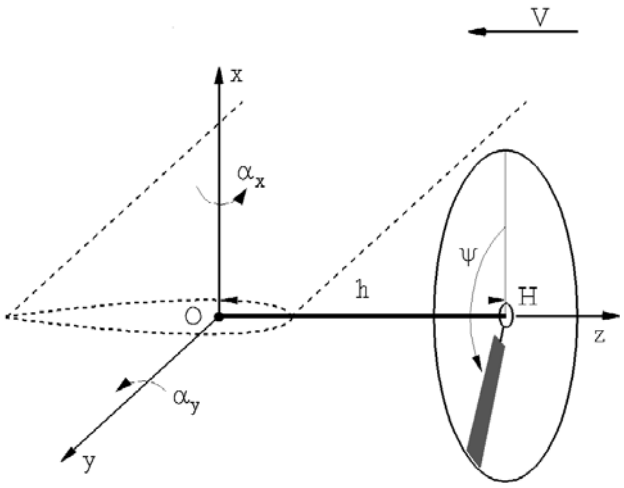


Figure 1. Pylon/prop-rotor system: the fixed frame of reference $\Re(0xyz)$ and the system degrees of freedom are indicated.

Symbols

$(\tilde{\ })$	Laplace domain
$(\dot{\ })$	non-dimensional time derivative
$(\ )^\circ$	trim state
$(\ )'$	perturbation wrt trim state

1.0 INTRODUCTION

The last years showed an increased interest in tiltrotors because, while having the VTOL capabilities of a helicopter, they have advantages over conventional helicopters in terms of cruise speed and operational range. The high-speed aeroelastic instability phenomenon known as whirl flutter is one of the limitations to cruise velocity for tiltrotors in airplane mode. The study of this kind of instability started in the early 1960s because of the loss of two aircraft caused by occurrence of prop-rotor whirl flutter[1,2]. That research activity showed that, for rigid-blade prop-rotors, this instability of the shaft-bearing-rotor system would occur as a low-frequency backward whirl mode, which is a mode motion in which the shaft whirls in the direction opposite to that of blade rotation. It was shown also that, for rotor configurations with flapping blades, additional vibrations could be generated by the high-frequency forward whirl mode[3]. Even when the system doesn't become unstable, these vibrations may induce fatigue phenomena on the rotor shaft bearings, which in turn may cause failure of the prop-rotor.

The recent interest in tiltrotor configurations has renewed research effort in whirl flutter analysis, with particular emphasis on the topic issues concerning structural modelling[4,6]. In these aircrafts, whirl flutter is caused by the coupling of the aerodynamic loads generated by the rotor blades with the wing elastic motion. The modelling of this phenomenon is not an easy task. The simulation of the interaction between prop-rotor and wing is a complex matter both because of kinetic and elastic couplings and because of aerodynamic unsteadiness and 3D interference effects. An accurate aerodynamic analysis of the wing/prop-rotor system would require the use of direct CFD simulation tools, with the drawback of a high computational effort. Thus, for preliminary design and control-law tailoring where simplified prediction models are more suitable, quasi-steady models combined with a strip theory approach or vortex line methods are often used to evaluate the aerodynamic loads acting on the prop-rotor blades[4,6].

In this work, aerodynamic models that are suitable for the aeroelastic stability analysis of pylon/prop-rotor systems are discussed. In particular, the influence of aerodynamic modelling on the prediction of whirl flutter instability boundaries is examined, including wake vorticity unsteadiness and 3D effects. The attention is focused on models that can conveniently be applied to preliminary design and control purposes. To this aim, the aeroelastic analysis is performed by means of reduced-order models (ROMs) obtained by following the methodology introduced in Ref. 7. These models allow the time-domain evaluation of the aerodynamic loads on prop-rotor blades as explicit functions of the system degrees of freedom and of a finite number of additional (aerodynamic) states. Although the coefficients appearing in these ROMs are periodic functions of time due to the pylon/prop-rotor (or wing/pylon/prop-rotor) kinetic interaction, the process of their identification requires only frequency-domain aerodynamic solutions[7]. When coupled with the structural operator these aerodynamic ROMs yield aeroelastic linear models that are suited for design and control-law applications because of their simple mathematical description and low computational cost, and are as accurate as the aerodynamic frequency-domain solver applied. Flutter detection is obtained through eigenvalue analysis. The approach outlined above for the identification of rotor aerodynamic ROMs could be considered an alternative way to the well known and widely-used approach presented in Refs 8 and 9, where the finite-state approximation is applied to the inflow on the rotor disk induced by the wake.

In addition to a quasi-steady model (for which there is no need to apply the methodology of Ref. 7, and that is here discussed for the sake of completeness) two unsteady aerodynamic solvers are considered. The first one is a 2D model based on the Theodorsen theory[10], that includes the lift deficiency to take into account the flow unsteadiness induced by the vorticity shedding process behind each prop-rotor blade (the effect of the returning wake below the blade is discussed in the next sections). The second frequency-domain solver considered is a boundary element method (BEM) for 3D, unsteady, potential flows, that has already been validated both for wings and helicopter rotors and is applicable to thick blades with arbitary shape (see, for instance, Ref. 11).

The corresponding aeroelastic operators are determined by coupling these aerodynamic models with a pylon/prop-rotor system in axial motion. Pylon inertia, damping and elastic restraint are introduced to model the dynamics of the engine mount structure (shaft bearings and pylon-nacelle links).

https://doi.org/10.1017/S0001924000002207 Published online by Cambridge University Press

2.0 STRUCTURAL PROP-ROTOR MODEL

The structural model included in the aeroelastic operator is based on rigid-body assumption for prop-rotor blades and follows the one used in Ref. 12. As mentioned above, the emphasis lies on the analysis of the influence of aerodynamic modelling on whirl flutter prediction, and such structural model has been chosen because, although simple, takes into account all the basic elements that play an important role in the aeroelastic phenomenon under examination. In particular, it allows the investigation of backward whirl mode stability boundaries[3,6].

The prop-rotor system (Fig. 1) is composed of a rigid-blade prop-rotor rigidly connected to a pylon that, in turn, is free to rotate in pitch and yaw about a pivot that is located at a distance h from the rotor hub. Damping and elastic restraints of the pylon motion are included in the pylon/prop-rotor system in order to simulate the dynamics of the engine mount structure, where damping and elastic actions arise when the system is subject to out-of-axis perturbations. In a fixed frame of reference, $\Re(0xyz)$, with the origin at the pylon pivot and the z-axis aligned with the pylon in its equilibrium, unperturbed axial-motion state, the general expression of the non-dimensional linearised equation of motion describing the dynamics of the pylon degree-of-freedom perturbations is given by

$$\mathbf{M}(\psi)\ddot{\boldsymbol{\alpha}} + \mathbf{C}(\psi)\dot{\boldsymbol{\alpha}} + \mathbf{K}\boldsymbol{\alpha} = \mathbf{m}_{aer}(\psi, \boldsymbol{\alpha}) \qquad \ldots (1)$$

where $\boldsymbol{\alpha} = \{\alpha_y\ \alpha_x\}^T$ is the vector of the yaw and pitch degrees of freedom (α_x and α_y, respectively), ψ is the azimuth position of the rotor, the time derivative is intended with respect to non-dimensional time (ψ), and $\mathbf{m}_{aer}$ is the vector of the moments on the pivot produced by the aerodynamic loads acting on the blades (pylon aerodynamic forces are neglected). The non-dimensional expression is obtained by dividing the equations by the factor $(N/2)I_b/\Omega^2$, where N denotes the number of prop-rotor blades, I_b the moment of inertia of one single prop-rotor blade with respect to the hub, and Ω denotes the prop-rotor angular velocity.

Mass matrix, **M**, and damping matrix, **C**, in Equation (1), in addition to the pylon terms, include also inertial contributions from the blades and this is the origin of their dependence on the rotor azimuth position. However, for prop-rotors having a number of blades $N \geq 3$ the combination of the contributions from each blade is such that these two matrices become constant (the ellipsoid of inertia of the prop-rotor is of circular type). Specifically, for $N = 2$, in Equation (1) one has

$$\mathbf{M} = \begin{bmatrix} \bar{I}_y + 1 + \mathrm{Cos}(2\psi) & -\mathrm{Sin}(2\psi) \\ -\mathrm{Sin}(2\psi) & \bar{I}_x + 1 - \mathrm{Cos}(2\psi) \end{bmatrix},$$

$$\mathbf{C} = \begin{bmatrix} \bar{C}_y - 2\mathrm{Sin}(2\psi) & -2[1 + \mathrm{Cos}(2\psi)] \\ 2[1 - \mathrm{Cos}(2\psi)] & \bar{C}_x + 2\mathrm{Sin}(2\psi) \end{bmatrix},$$

$$\mathbf{K} = \begin{bmatrix} \bar{K}_y & 0 \\ 0 & \bar{K}_x \end{bmatrix}$$

whereas, for $N \geq 3$, mass and damping matrices become

$$\mathbf{M} = \begin{bmatrix} \bar{I}_y + 1 & 0 \\ 0 & \bar{I}_x + 1 \end{bmatrix}, \mathbf{C} = \begin{bmatrix} \bar{C}_y & -2 \\ 2 & \bar{C}_x \end{bmatrix}.$$

In the expression above, $\bar{K}_x$, $\bar{K}_y$ denote the non-dimensional spring restraints of pylon motion about the pivot, $\bar{C}_x$, $\bar{C}_y$ denote the non-dimensional yaw and pitch damping, whereas $\bar{I}_x$, $\bar{I}_y$ denote the non-dimensional pylon yaw and pitch moments of inertia (with inclusion of rotor mass contribution, that is equivalent to that of a point mass located at the rotor hub).

The aerodynamic terms in the right hand side of Equation (1) are given by the combination of the contributions from forces and moments acting on each blade of the rotor. Denoting with $\bar{M}_n^f$, and $\bar{M}_n^t$, respectively flap and torsion aerodynamic hub non-dimensional moments on the n-th blade, and with $\bar{F}_n$ the in-plane aerodynamic non-dimensional force on the n-th blade (orthogonal to the radial direction, along which aerodynamic loads are assumed to be negligible), the aerodynamic contribution to the prop-rotor perturbation dynamics is given by (see Fig. 2)

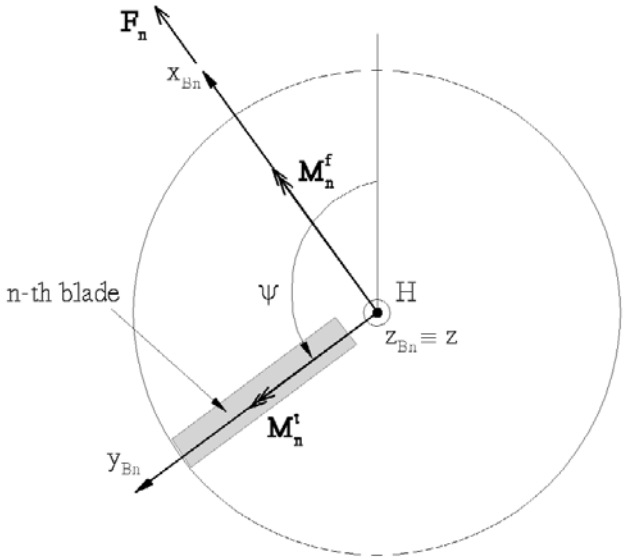


Figure 2. Hub moments and forces on the n-th blade: blade rotating frame of reference $\Re(Hx_{Bn}y_{Bn}z_{Bn})$ is indicated.

$$\mathrm{m}_{aer}(\boldsymbol{\psi}, \boldsymbol{\alpha}) = \begin{Bmatrix} \sum_n^N \left[-\bar{M}_n^f\, \mathrm{Cos}(\boldsymbol{\psi}) + (\bar{M}_n^t + \bar{F}_n\, \bar{h})\mathrm{Sin}(\boldsymbol{\psi}) \right] \\ \sum_n^N \left[\bar{M}_n^f\, \mathrm{Sin}(\boldsymbol{\psi}) + (\bar{M}_n^t + \bar{F}_n\, \bar{h})\mathrm{Cos}(\boldsymbol{\psi}) \right] \end{Bmatrix} \qquad \ldots (2)$$

with $\bar{h} = h/R$, where R represents the rotor radius. The description of the aerodynamic forcing terms appearing above is the subject of the next section.

3.0 AERODYNAMIC REDUCED-ORDER MODELS FOR PROP-ROTOR AEROELASTICITY

Several aerodynamic models may be applied in prediction tools concerning aeroelasticity of pylon/prop-rotor systems. The wide range of possible choices goes from 3D CFD solvers to 2D quasi-steady models. However, here the emphasis is on those operators that, combining simplicity with a good level of accuracy, are convenient from the design point of view. Here, three aerodynamic models are analysed and applied in the identification of whirl flutter boundaries of pylon/prop-rotor structures. In addition to the standard 2D quasi-steady model that is included for comparison, a reduced-order model based on the 2D Theodorsen theory and a reduced-order model based on a 3D unsteady BEM solver are introduced.

https://doi.org/10.1017/S0001924000002207 Published online by Cambridge University Press

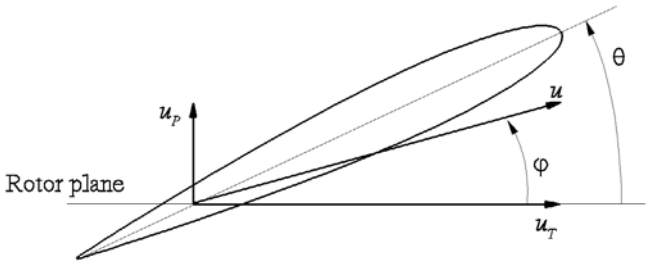


Figure 3. Blade section velocities with respect to fluid at the 3/4-chord point (in-plane, u_T and out-of-plane, u_P) and blade section pitch angle (ϑ).

3.1 Quasi-steady aerodynamics

This is a widely-used model that is based on the very-low-frequency approximation of the Theodorsen theory[10], where the lift deficiency function is assumed to be equal to one. The section loads predicted by this approach are integrated along the blade to get the right-hand-side terms in Equation (2).

Denoting with u_T and u_P, respectively, the in-plane and the out-of-plane blade section velocities with respect to fluid at the 3/4-chord point, with ϑ the blade section pitch angle, and with φ the inflow angle (see Fig. 3), following Ref. 12, the in-plane and the out-of-plane aerodynamic section loads are given by (see also Ref. 6)

$$f^{in} = L\,\mathrm{Sin}(\varphi) + D\,\mathrm{Cos}(\varphi),\; f^{out} = L\,\mathrm{Cos}(\varphi) - D\,\mathrm{Sin}(\varphi) \qquad \ldots (3)$$

where

$$L = \frac{1}{2}\rho\, c\,(u_T^2 + u_P^2)\, a\,(\vartheta - \varphi),\; D = \frac{1}{2}\rho\, c\,(u_T^2 + u_P^2)\, c_D \qquad \ldots (4)$$

are lift and drag forces, respectively. In the equation above, ρ is the air density, c is the section chord, a is the lift curve slope, c_D is the section drag coefficient, whereas $\varphi = \mathrm{Tan}^{-1}(u_P/u_T)$. The comparison of this section load model with the Theodorsen theory[10] reveals that in Equation (4) the noncirculatory (unsteady) terms are neglected. In addition, the aerodynamic torque moment transmitted to the hub is assumed to be zero (note that, for the lift deficiency function equal to one the circulatory aerodynamic torque moment is zero about the mid-chord point, whereas under steady-state assumption the total aerodynamic torque moment is equal to zero about the 1/4-chord point).

To determine the expressions of the blade loads to be included in Equation (2), the combination of Equations (3) and (4) has to be written in terms of the perturbation velocity about a trim state, and the linearised version of it has to be derived. This yields the following relationship between forces and perturbation variables

$$\begin{Bmatrix} f^{in} \\ f^{out} \end{Bmatrix} = \rho\, a\, c\, \mathbf{H}(\vartheta, c_D, u_T^0, u_P^0) \begin{Bmatrix} u_T' \\ u_P' \end{Bmatrix}$$

where, for an axial-flow trim state, $u_T^0 = \Omega r$ and $u_P^0 = V + v_i$, with r denoting the spanwise section blade location, V denoting the axial velocity and v_i denoting the velocity induced by the prop-rotor wake. The final steps to get the blade loads to be included in the dynamics equations consist of expressing the perturbation velocity components in terms of the yaw and pitch degrees of freedom of the pylon, followed by integration along the blade span. The resulting expressions are

$$\begin{Bmatrix} \bar{F}_n \\ \bar{M}_n^f \end{Bmatrix} = \frac{2}{N}\gamma \begin{Bmatrix} \int_0^1 \bar{f}_n^{in}\,\mathrm{d}\bar{r} \\ \int_0^1 \bar{f}_n^{out}\,\mathrm{d}\bar{r} \end{Bmatrix} = \frac{2}{N}\gamma\,[\mathbf{A}_1(\psi_n)\dot{\boldsymbol{\alpha}} + \mathbf{A}_0(\psi_n)\boldsymbol{\alpha}\,] \qquad \ldots (5)$$

where $\gamma = \rho acR^4/I_b$ is the Lock number and $\mathbf{A}_0$, $\mathbf{A}_1$ are the periodic matrices that relate the structural degrees of freedom to the corresponding aerodynamic loads. Their dependence on the blade azimuth position comes from the kinetic relation between blade section velocity components and pylon motion[12]. Combining Equation (5) (including the assumption $\bar{M}_n^t = 0$) with Equations (1) and (2) yields a pylon/prop-rotor aeroelastic model that can be used to determine whirl flutter boundaries. Akin to the structural contribution terms, the matrices given by combination of Equation (5) with Equation (2) are constant for $N \geq 3$, whereas the aerodynamic contribution contains periodic-coefficient terms for $N = 2$. Therefore, the stability analysis requires the solution of a classical eigenvalue problem for $N \geq 3$, whereas the Floquet theory[13] is applied for studying two-bladed prop-rotors.

3.2 2D unsteady aerodynamics

The 2D, unsteady model differs from the quasi-steady one in that, in addition to the inclusion of the noncirculatory terms, it takes into account the effects of the unsteady shed vorticity convected along the wake behind each prop-rotor blade, which plays a fundamental role in the evolution of the flow field around the airfoil. These effects appear in the mathematical model of the aerodynamic loads in the form of a frequency-dependent lift deficiency function scaling the circulatory terms. Here, the Theodorsen theory[10] is applied, in that the effects of the returning wake (considered, for instance, in the formulation introduced by Loewy[14]) are assumed to be negligible for the prop-rotor advance ratios that are of interest in the analysis of backward whirl flutter[3].

From the Theodorsen theory[10], unsteady lift and torque moment about the 1/4-chord point can be expressed as

$$L = \frac{1}{2}\rho\, a\, c\left[\frac{c}{4}\left(-\dot{u}_P\,\mathrm{Cos}(\vartheta) + \dot{u}_T\,\mathrm{Sin}(\vartheta) - \frac{c}{4}\dot{\varepsilon}\right) + C(k)(u_T^2 + u_P^2)(\vartheta - \varphi)\right] \qquad \ldots (6)$$

$$M_{1/4} = -\frac{1}{2}\rho\, a\, c\left(\frac{c}{4}\right)^2\left[\mathrm{Cos}(\vartheta)(u_T\,\varepsilon - \dot{u}_P) + \mathrm{Sin}(\vartheta)(u_P\,\varepsilon + \dot{u}_T) - \frac{c}{8}\dot{\varepsilon}\right] \qquad \ldots (7)$$

where ε is the angular velocity of the blade section in the rotating frame and $C(k)$ is the lift deficiency function that depends on the reduced frequency, $k = \omega c/2\Omega r$ (see Ref. 10). The drag force is still given by the expression in Equation (4).

In order to determine the corresponding aerodynamic operator to be included in Equation (1), Equation (6) and the drag in Equation (4) are combined with Equations (3), u_T, u_P and ε are perturbed about their axial-flow steady-state trim and the linearised expressions of the in-plane and out-of-plane forces, as well as that of the torque moment are retained. However, because of the presence of the lift deficiency function that has a transcendental dependence on the reduced frequency, these expressions are not convenient for direct inclusion in the dynamics equations to be applied for stability analysis purposes. Thus, the aerodynamic model to be included in Equation (1) is derived following the methodology presented in Ref. 7 which allows the identification of an aerodynamic ROM for prop-rotors starting from a solution for perturbative problems. The first steps of it consist of (*i*) expressing blade section perturbation velocity components u_T', u_P' and ε' in terms of the six rotating-frame velocity components of the rotor rigid-body motion (v_1, v_2, v_3, ω_1, ω_2, ω_3), (*ii*) integrating along the blade span and (*iii*) transforming into frequency domain. For each blade, this procedure yields a [3×6] transcendental transfer function matrix, **E**, for which

https://doi.org/10.1017/S0001924000002207 Published online by Cambridge University Press

$$\tilde{\mathbf{f}}_n = \begin{Bmatrix} \tilde{F}_n \\ \tilde{M}_n^f \\ \tilde{M}_n^t \end{Bmatrix} = \mathbf{E}_n(s) \begin{Bmatrix} \tilde{v}_i \\ \tilde{\omega}_i \end{Bmatrix} = \mathbf{E}_n(s)\,\tilde{\mathbf{v}} \quad \ldots (8)$$

where s is the complex reduced frequency and ~ denotes frequency transformation. Note that, the rotating frame of reference is defined, at each blade azimuth position, as the frame of reference $\Re(Hx_{Bn}y_{Bn}z_{Bn})$ rigidly connected with a reference blade (see Fig. 2).

Next, in order to get a finite-state description in the time domain (transcendental terms in frequency domain would give rise to an infinite-dimension state space problem in the time domain), matrix is approximated through the following rational matrix expression

$$\mathbf{E}_n(s) \approx s\,\mathbf{A}_1 + \mathbf{A}_0 + \mathbf{C}[s\,\mathbf{I} - \mathbf{A}]^{-1}\mathbf{B} \quad \ldots (9)$$

where $\mathbf{A}_1$, $\mathbf{A}_0$, $\mathbf{A}$, $\mathbf{B}$ and $\mathbf{C}$ are real, fully populated matrices. Matrices $\mathbf{A}_1$ and $\mathbf{A}_0$ have dimensions [3×6], $\mathbf{A}$ is a [N_a× N_a] matrix containing the N_a poles included in the approximating expression, $\mathbf{C}$ is a [3 × N_a] matrix, while $\mathbf{B}$ has dimensions [N_a × 6] (see Ref. 7). Then, combining Equation (9) with Equation (8) and transforming into time domain yields the following constant-coefficient expression relating the blade velocity components (and their first time derivatives) with the corresponding unsteady aerodynamic forces

$$\mathbf{f}_n(t) = \mathbf{A}_1\,\dot{\mathbf{v}} + \mathbf{A}_0\,\mathbf{v} + \mathbf{C}\,\mathbf{r} \quad \ldots (10)$$

with

$$\dot{\mathbf{r}} = \mathbf{A}\,\mathbf{r} + \mathbf{B}\,\mathbf{v} \quad \ldots (11)$$

where $\mathbf{r}$ is the column matrix that collects the N_a additional aerodynamic states associated with the poles included in the approximating aerodynamic matrix [a consequence of the presence of the lift deficiency function in matrix $\mathbf{E}(s)$]. The aerodynamic ROM to be included in Equation (1) is obtained by combining Equations (10) and (11) with the periodic-coefficient kinetic relationship between the rotor velocity components, $\mathbf{v}$, and the pylon degrees of freedom, $\boldsymbol{\alpha}$,

$$\mathbf{v}(t) = \mathbf{K}_1(\Omega, h, t)\,\dot{\boldsymbol{\alpha}} + \mathbf{K}_0(V, \Omega, t)\,\boldsymbol{\alpha} \quad \ldots (12)$$

The resulting expression reads

$$\mathbf{f}_n(t) = \mathbf{D}_2(t)\,\ddot{\boldsymbol{\alpha}} + \mathbf{D}_1(t)\,\dot{\boldsymbol{\alpha}} + \mathbf{D}_0(t)\,\boldsymbol{\alpha} + \mathbf{C}\,\mathbf{r}$$

with

$$\dot{\mathbf{r}} = \mathbf{A}\,\mathbf{r} + \mathbf{H}_1(t)\,\dot{\boldsymbol{\alpha}} + \mathbf{H}_0(t)\,\boldsymbol{\alpha}$$

where the periodic matrices have been defined in Ref. 7. Note that the outlined ROM identification procedure does not introduce any novel aerodynamics unsteady model: it simply allows the derivation of a finite-state form of the blade aerodynamic loads. This methodology can be applied to different unsteady aerodynamic solvers (the same procedure will be used in the next section combined with a BEM solver) given that the aerodynamic loads are expressed in the frequency domain.

Finally, combining the equations above with Equations (2) and (1) yields the periodic-coefficient finite-state aeroelastic operator based on the Theodorsen model for the prediction of the unsteady aerodynamic loads. This procedure yields an operator with periodic coefficient terms regardless of the number of prop-rotor blades, because of the inclusion of the additional aerodynamic states. However, it is worth observing that the application of the multiblade co-ordinate transformation would reduce it into a constant coefficient system.

3.3 BEM solver for 3D potential flows

Next, in order to examine the 3D aerodynamics effects on the prediction of the stability boundaries, an aerodynamic ROM based on a boundary integral equation formulation for potential, unsteady flows is applied. It has extensively been described in Ref. 7 and is briefly outlined in the following for the sake of completeness.

Consider a lifting body moving in an inviscid, incompressible flow. The velocity of the fluid particles may be expressed in terms of a potential function, ϕ, such that $\boldsymbol{v}_f = \nabla\phi$. Combination with the mass conservation law yields the Laplace equation for the potential, $\nabla^2\phi = 0$, that, through application of a boundary integral equation formulation, has the frequency-domain solution given by

$$\frac{1}{2}\tilde{\phi}(\mathbf{x}_*) = \int_{S_B}\left(\tilde{\mathbf{v}}_B^T\,\mathbf{n}\,G - \tilde{\phi}\frac{\partial G}{\partial n}\right)\mathrm{d}S(\mathbf{x}) - \int_{S_W}\Delta\tilde{\phi}^{TE}\,e^{-s\tau}\frac{\partial G}{\partial n}\mathrm{d}S(\mathbf{x}) \quad \ldots (13)$$

where S_B denotes the body surface, S_W denotes the wake surface, $G = -1/4\pi\,\|\mathbf{x} - \mathbf{x}_*\|$ is the unit source solution of the Laplace equation, whereas τ is the time taken by a wake material point to move from the trailing edge to the current position. In addition, $\boldsymbol{v}_B$ denotes body velocity (the one induced by the perturbation motion, for the stability problem under examination), $\mathbf{n}$ denotes body outward unit normal, and $\Delta\phi$ is the jump of potential across the wake (see Ref. 11 for further details). Numerical solution of Equation (13) is evaluated from its algebraic approximation, that is derived discretising the body surface into N_B quadrilateral panels and the wake surface into N_W quadrilateral panels. Assuming ϕ, $\mathbf{v}_B^T\mathbf{n}$ and $\Delta\phi$ constant over each panel [i.e. using a zeroth-order boundary element method (BEM)] and satisfying Equation (13) at the $N_c = N_B$ centres of the panels (collocation points) yields an algebraic approximation that may be written in the matrix form, $\tilde{\boldsymbol{\varphi}} = \mathbf{E}_\phi(s)\tilde{\boldsymbol{\chi}}$, where $\tilde{\boldsymbol{\varphi}}$ and $\tilde{\boldsymbol{\chi}}$ are the column matrices collecting, respectively, the values of ϕ and $\mathbf{v}_B^T\mathbf{n}$ at the collocation points, whereas $\mathbf{E}_\phi$ is a [$N_c \times N_c$] matrix collecting all the aerodynamic coefficients coming from the discretisation of Equation (13)[7]. Then, defining the matrix $\mathbf{E}_p(s)$ relating the potential field with the pressure on the blade (from Bernoulli's theorem), along with the matrix $\mathbf{E}_f$ relating pressure to forces, and the matrix $\mathbf{E}_{BC}$ relating boundary conditions, $\boldsymbol{\chi}$, to the rotating-frame perturbation velocity components of the rotor rigid-body motion, $\boldsymbol{v}$, for each blade one obtains a frequency-domain aerodynamic operator that is formally identical to that in Equation (8), with the matrix $\mathbf{E}_n$ given by Ref. 7.

$$\mathbf{E}_n(s) = \mathbf{E}_f\,\mathbf{E}_p(s)\,\mathbf{E}_\phi(s)\,\mathbf{E}_{BC}$$

(drag effects are included by using the expression in Equation (4)). Akin to the approach based on the Theodorsen theory, these aerodynamic transfer functions are transcendental functions of the complex reduced frequency because of the wake unsteady terms [see the wake convective delay terms appearing in Equation (13)]. Hence, the aerodynamic ROM to be coupled with Equation (1) is identified following the same procedure outlined above for the Theodorsen model. Also in this case, the aerodynamic ROM contains additional aerodynamic states and the resulting aeroelastic operator has periodic-coefficient terms, regardless of the number of prop-rotor blades. Similarly, the introduction of multiblade coordinates would transform it into a constant-coefficient form.

The BEM solver described above can be applied either by using a simple helicoidal wake shape or a more realistic distorted wake shape given by a free-wake analysis of the steady-state trim configuration. It consists of the application of a time-domain BEM aerodynamic solver in which the wake geometry is calculated as a part of the flowfield solution by imposing that the wake points be aligned with the local flow field (see, for instance, Ref. 11). The effect of the use of different wake shapes will be analysed in the following section.

https://doi.org/10.1017/S0001924000002207 Published online by Cambridge University Press

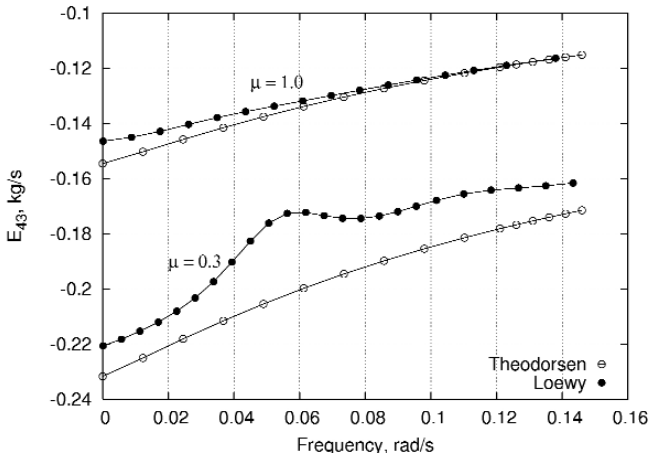


Figure 4. Transfer function between ω_1 and blade flapping moment (real part).

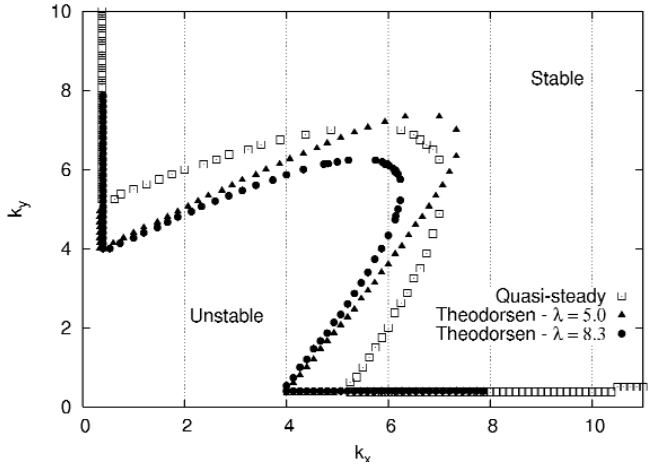


Figure 5. Whirl flutter stability boundaries: three-bladed rotor, μ = 1·0.

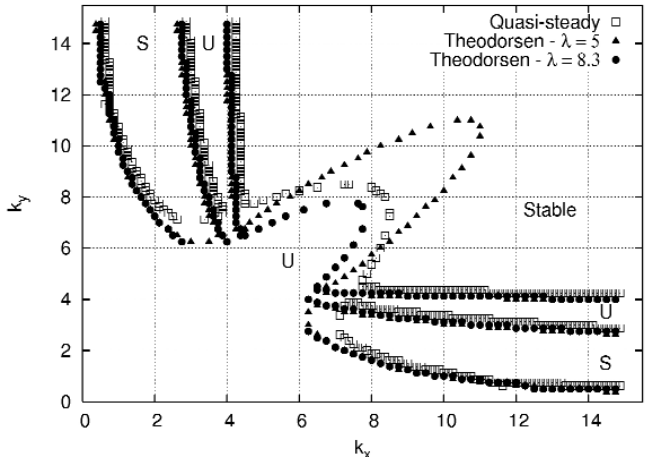


Figure 6. Whirl flutter stability boundaries: two-bladed rotor, μ = 1·0.

4.0 NUMERICAL RESULTS

Numerical investigation has been performed in order to clarify limits and advantages of the different aerodynamic models described above for the prediction of pylon/prop-rotor whirl flutter. The results of this aeroelastic analysis consist of a parametric study with respect to the values of pylon motion spring restraints and will be presented in terms of stability boundaries in the $\bar{K}_x$, $\bar{K}_y$ plane. The pylon/prop-rotor test case examined is that considered in Ref. 12, with the structural parameters $\bar{h} = 0{\cdot}3$, $\bar{I}_x = 2$, $\bar{I}_y = 2$, $\bar{C}_x = 0$, and $\bar{C}_y = 0$ (see Section 2).

First, consider the 2D unsteady aerodynamic modelling examined in this work. As mentioned in Section 3, in order to include the effects of the unsteady shed vorticity convected along the wake behind and below each prop-rotor blade, the Loewy lift deficiency function should be used in the model. However, for prop-rotor applications concerning high advance ratios (as in the present analysis), the effects of the unsteady vorticity in the wake are satisfactorily described through the Theodorsen lift deficiency function, thus taking into account only the wake portion behind each prop-rotor blade section. To demonstrate this, consider a hub frame of reference $\Re(Hxyz)$ having the z-axis aligned with the rotor shaft and the y-axis aligned with the rotor reference blade.

For a three-bladed prop-rotor, Fig. 4 shows the values of the real part of the transfer function $E_{43}(k)$ between the rotor angular velocity about the x-axis and the blade flapping moment, computed using the Theodorsen model and the Loewy model (i.e. that using the Loewy lift deficiency function) at advance ratios $\mu = 0{\cdot}3$ and $\mu = 1{\cdot}0$ ($\mu = V/\Omega R$). The two results tend to coincide for high values of μ. When μ decreases (together with the wake pitch length) the effect of the vorticity shed below the reference blade by the other rotor blades becomes significant and the transfer function evaluated using the Loewy model presents an oscillatory trend thus the differences with the Theodorsen model increase. However, the maximum relative difference remains not higher than 15% and further numerical investigation has shown that it has a negligible effect on the stability analysis. For this reason, in the rest of the numerical investigation, the unsteady 2D aerodynamic solver will be obtained through the Theodorsen theory.

Next, the whirl flutter boundaries obtained using the 2D quasi-steady and unsteady aerodynamic models are shown. Note that, for the 2D quasi-steady solver, Lock number, γ, and advance ratio are the only parameters needed to describe the flight conditions, whereas the unsteady models require also the knowledge of the blade aspect ratio, $\lambda = R/c$, because of the presence of noncirculatory terms and lift deficiency functions. The stability boundaries predicted for a three-bladed rotor for $\gamma = 4$ and $\mu = 1{\cdot}0$ are shown in Fig. 5.

Results obtained using the 2D quasi-steady model are compared with those predicted by the Theodorsen approach. The unsteady aerodynamic solver has been applied considering two values of the blade aspect ratio (namely $\lambda = 5$ and $\lambda = 8{\cdot}3$). The whirl flutter boundaries can be divided into three branches. The central branch is a parabola with the axis parallel to the 45°-line on the $\bar{K}_x$, $\bar{K}_y$ plane (because of isotropic pylon inertias), and position of the vertex depending on the advance ratio. The region inside this parabola corresponds to unstable configurations. The other two branches are almost parallel to the axes and define the divergence boundaries. Figure 5 shows that the use of the simple 2D quasi-steady formulation overpredicts the unstable region with respect to that given by the 2D unsteady model (thus giving conservative results) only for the highest value of λ. Note that the blade aspect ratio $\lambda = 8{\cdot}3$ has been chosen in that it is related to the Boeing prop-rotor analysed in Ref. 12.

In the same flight conditions, Fig. 6 shows aeroelastic predictions for a two-bladed rotor. In this case, the stability boundaries have a different shape with respect to the three-bladed rotor case, since divergence-like instabilities may occur at 1/*rev* frequency, thus determining two more branches of the boundary. This fact is mainly induced by the lack of axisymmetry of the system that produces periodic inertial contributions (see Section 2). Akin to the three-bladed case, the quasi-steady aerodynamic model predicts a greater unstable region with respect to the unsteady aerodynamic model for higher-aspect ratio blades, whereas the contrary is observed for lower-aspect ratio blades.

https://doi.org/10.1017/S0001924000002207 Published online by Cambridge University Press

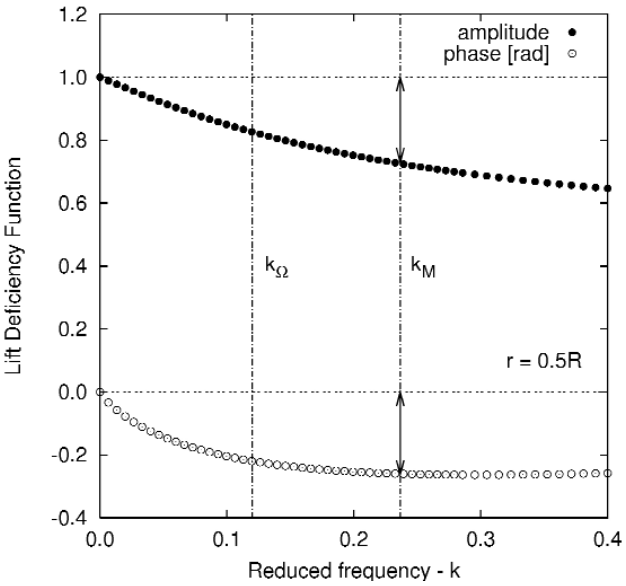


Figure 7. Lift deficiency function corresponding to blade motion frequency: $r/R = 0{\cdot}5$.

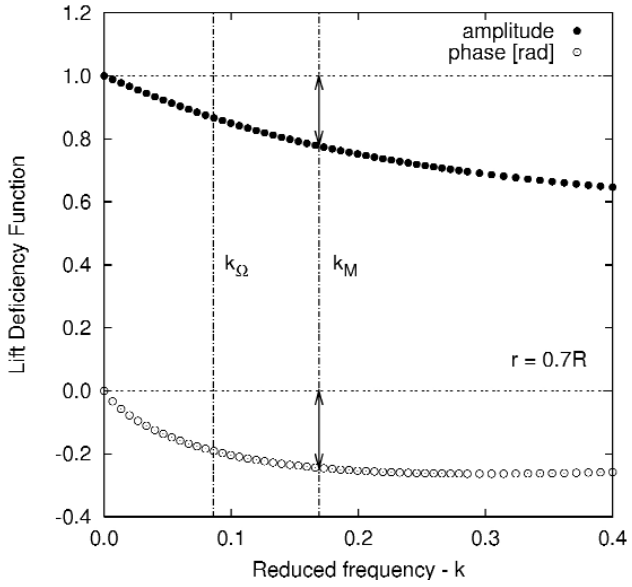


Figure 8. Lift deficiency function corresponding to blade motion frequency: $r/R = 0{\cdot}7$.

Note that, the results presented in Figs 5 and 6 obtained by using the 2D quasi-steady aerodynamic model coincide with those given for a prop-rotor in Ref. 12. As already observed by many authors (see, for instance, Refs 3 and 6), for a rigid-blade rotor, whirl flutter instability invariably involves the low-frequency backward whirl mode. Thus, the influence of unsteady aerodynamics on whirl flutter stability boundaries seems to be somewhat surprising. To clarify this point, it is worth observing that the rotor aerodynamic loads (that are the forcing terms of the pylon equations of motion) are characterised by the blade motion frequency that, in turn, is the result of the combination of the rotation about rotor axis and pylon motion. Therefore, although the whirl flutter instability is dominated by a low-frequency pylon motion, the corresponding blade motion has a higher frequency content given by the combination of the rotor revolution frequency Ω with that of the pylon motion, ω_α Then, the

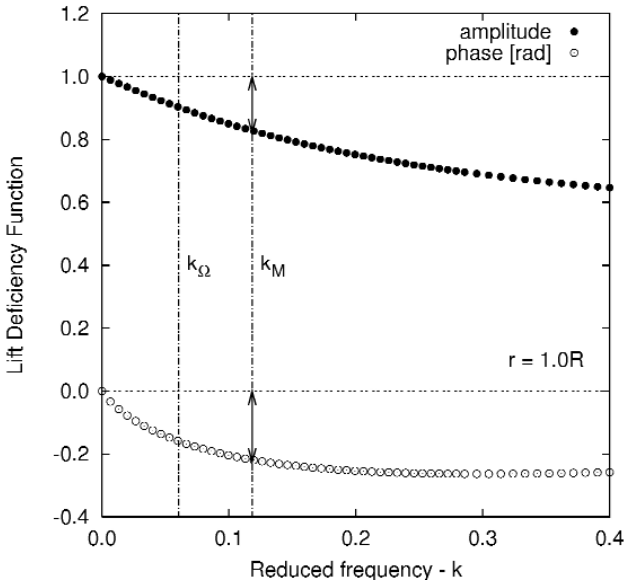


Figure 9. Lift deficiency function corresponding to blade motion frequencies: $r/R = 1{\cdot}0$.

effect of such higher frequency motion in the whirl flutter is examined by considering the stability boundaries for the three-bladed rotor in Fig. 5. For $\bar{K}_x = 6{\cdot}0$ and $\lambda = 8{\cdot}3$ the flutter boundary predicted by the 2D unsteady model is at $\bar{K}_y = 4{\cdot}4$ with the reduced frequency of the unstable eigenvalue equal to $k_F = \omega_F c/2\Omega R = 0{\cdot}058$. Combining it with the rotor rotational velocity yields a high reduced frequency $k_M = \omega_M c/2\Omega r$ distribution along blade span for which the corresponding Theodorsen lift deficiency function amplitude and phase evaluated at $r/R = 0{\cdot}5$, $r/R = 0{\cdot}7$ and $r/R = 1{\cdot}0$ are depicted in Figs 7-9 (where $k_\Omega = c/2r$). In particular, the high frequency $\omega_M = \Omega + \omega_\alpha$ appears in the blade motion spectrum.

The discrepancies between the assumption $C(k) = 1$ and the exact computed values at $k = k_M$ explain the differences in the stability boundaries predicted by using the 2D quasi-steady and the 2D unsteady aerodynamic model (see Figs 5 and 6). Since the local reduced frequency along blade span decreases as the blade aspect ratio increases, the described phenomenon is even more evident for lower-aspect ratio blades, as demonstrated by Figs 5 and 6 for $\lambda = 5{\cdot}0$ (this consideration explains also the evident dependence of the 2D unsteady results on the blade aspect ratio).

Next, the effect of the advance ratio on the whirl flutter boundaries is investigated.

Figures 10 and 11 show the stability predictions for a three-bladed and a two-bladed rotor, respectively, for $\mu = 0{\cdot}3$. The decrease of the advance ratio from $\mu = 1{\cdot}0$ to $\mu = 0{\cdot}3$ causes a significant reduction of the unstable regions, thus highlighting that the whirl flutter is an aeroleastic instability that occurs at high advance ratio. In this case, the 2D quasi-steady and unsteady aerodynamic models give very similar results with those from the 2D quasi-steady formulation slightly underpredicting the 1/*rev* divergence in the two-bladed case. Note that, for low-advance ratio flight conditions, the blade motion frequencies corresponding to a stability boundary point yields lower values of k_M with respect to those arising at high-advance ratios conditions. This is reflected in the similarity between the stability boundaries predicted by using $C(k) = 1$ (quasi-steady) and by the unsteady aerodynamic model.

Now, the aerodynamic ROM based on the BEM solver outlined in Section 3.3 is applied. First the wake is assumed to have a helicoidal shape with pitch given by the advance ratio, i.e. the wake coincides with the surface swept by the blade trailing edge during its unperturbed motion. The rational matrix approximation of the BEM

https://doi.org/10.1017/S0001924000002207 Published online by Cambridge University Press

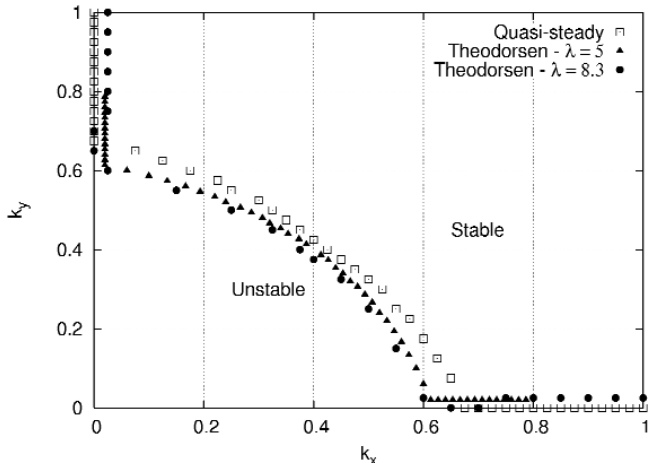


Figure 10. Whirl flutter stability boundaries: three-bladed rotor, μ = 0·3.

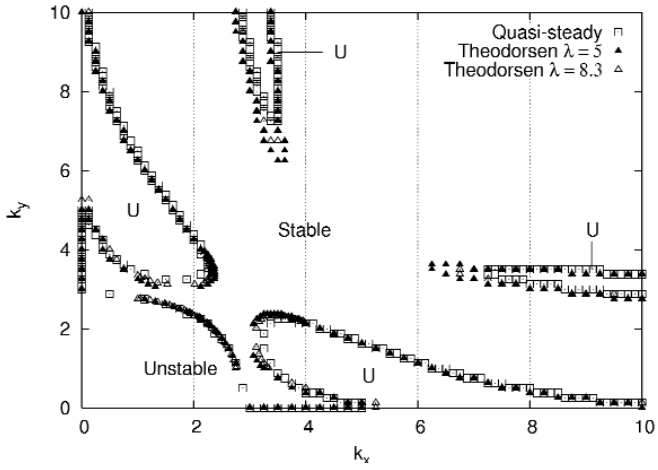


Figure 11. Whirl flutter stability boundaries: two-bladed rotor, μ = 0·3.

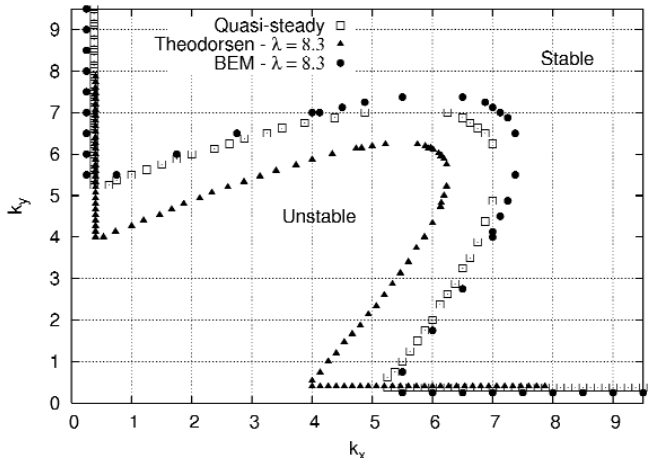


Figure 12. Whirl flutter stability boundaries: three-bladed rotor, μ = 1·0.

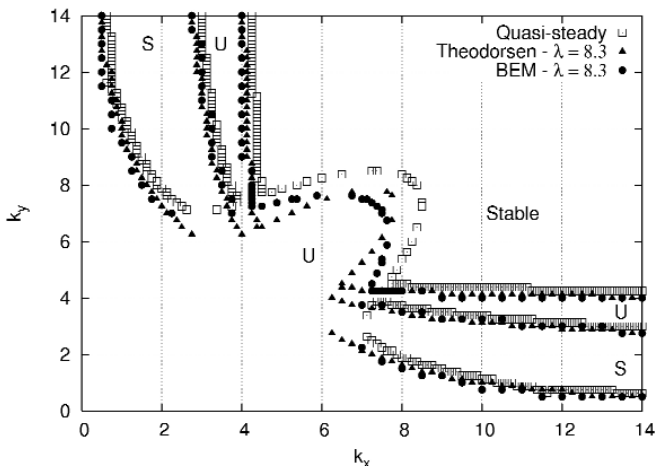


Figure 13. Whirl flutter stability boundaries: two-bladed rotor, μ = 1·0.

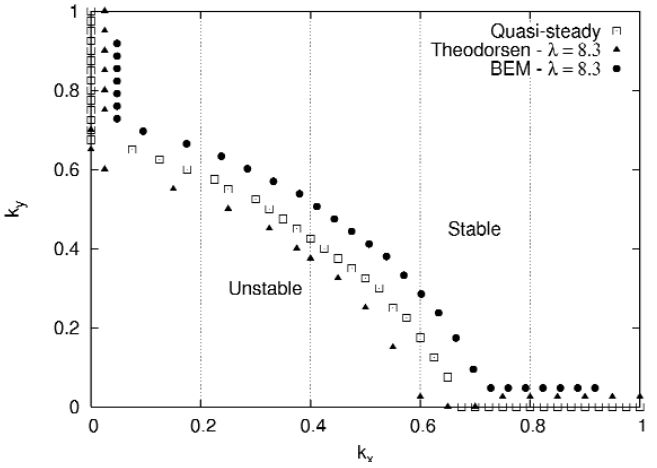


Figure 14. Whirl flutter stability boundaries: three-bladed rotor, μ = 0·3.

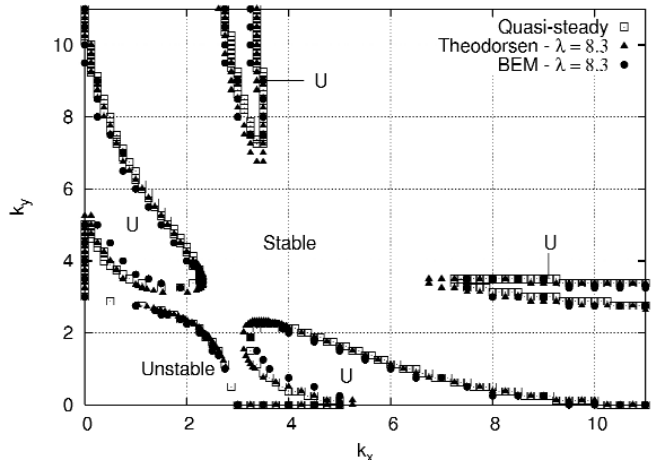


Figure 15. Whirl flutter stability boundaries: two-bladed rotor, μ = 0·3.

aerodynamic transfer functions has been validated in the past (see, for instance, Ref. 7).

In Fig. 12 numerical predictions obtained using the 3D unsteady BEM solver are compared with those obtained by the 2D solvers, for a three-bladed rotor with λ = 8·3 and μ = 1·0, whereas the same comparison is depicted in Fig. 13 for the two-bladed rotor. For these configurations the 2D aerodynamic unsteady model causes a general underprediction of the unstable regions while the 2D quasi-steady one underpredicts instability for the three-bladed prop-rotor, but yields conservative results for the two-bladed one.

https://doi.org/10.1017/S0001924000002207 Published online by Cambridge University Press

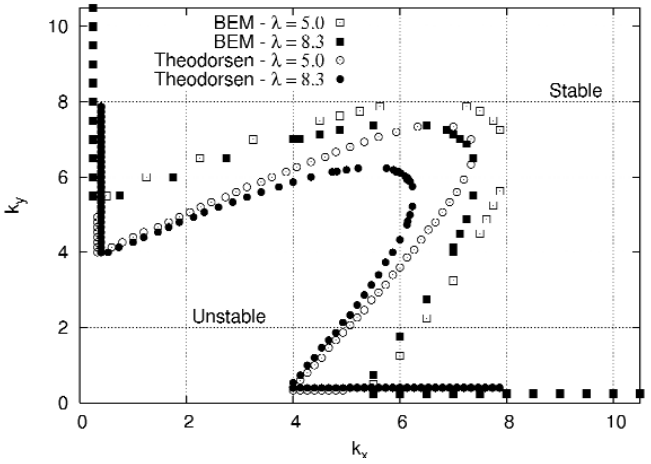


Figure 16. Whirl flutter stability boundaries: effect of blade aspect ratio in 2D and 3D aerodynamic models for a three-bladed rotor, μ = 1·0.

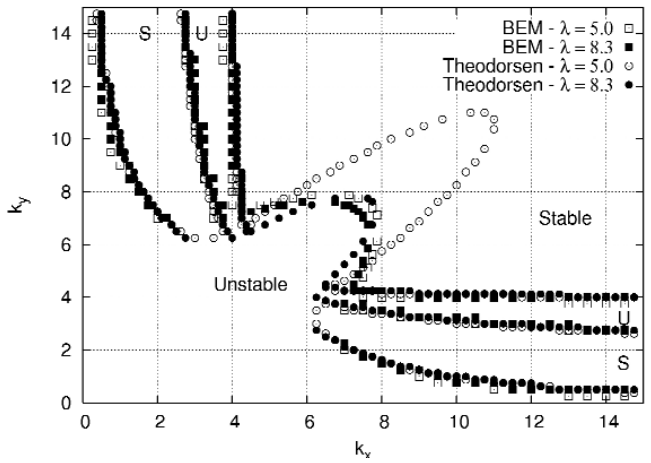


Figure 17. Whirl flutter stability boundaries: effect of blade aspect ratio in 2D and 3D aerodynamic models for a two-bladed rotor, μ = 1·0.

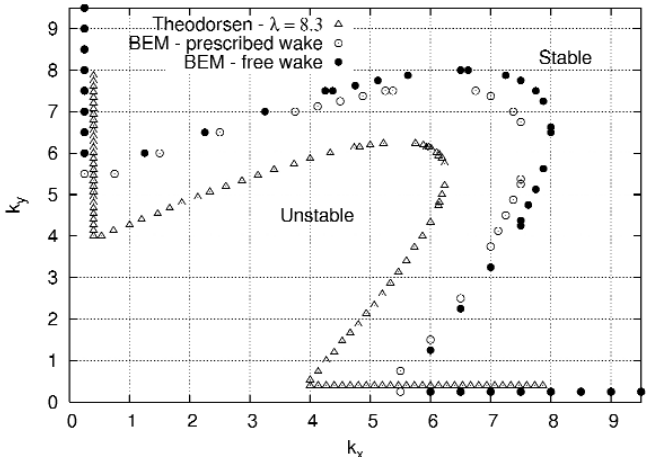


Figure 18. Whirl flutter stability boundaries: effect of a distorted wake-shape in the 3D aerodynamic model for a three-bladed rotor, μ = 1·0, λ = 8·3.

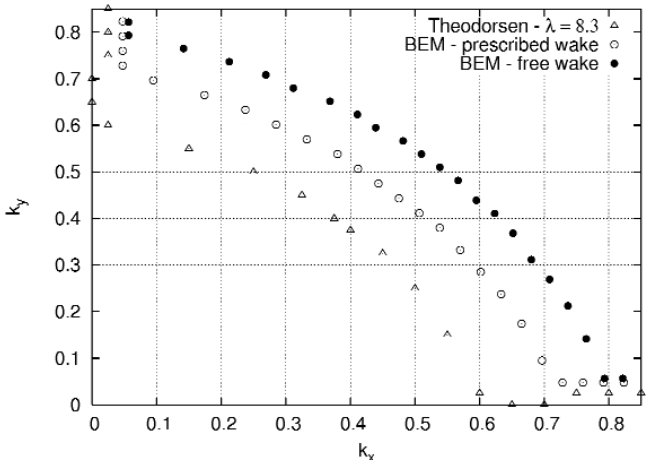


Figure 19. Whirl flutter stability boundaries: effect of a distorted wake-shape in the 3D aerodynamic model for a three-bladed rotor, μ = 0·3, λ = 8·3.

Figures 14 and 15 show predictions for μ = 0·3. Also in this case, the use of a 2D aerodynamic solver yields an underprediction of the unstable region with respect to the results obtained using a 3D unsteady BEM solver for the three-bladed solver, whereas for the two-bladed rotor all the aerodynamic solvers give similar results in terms of stability boundaries.

Next, the effect of the blade aspect ratio on the stability boundaries predicted using the Theodorsen model is compared with that on the flutter prediction from the 3D BEM model.

Figure 16 shows the results for a three-bladed rotor at μ = 1·0, for λ = 5·0 and λ = 8·3 for both aerodynamic models. An increase in the blade aspect ratio causes a reduction of the flutter regions. However, it increases the underprediction of the unstable regions resulting from the application of the 2D unsteady solver. Figure 17 shows the same analysis for the two-bladed rotor. Also in this case an increase of the blade aspect ratio causes a reduction of the flutter region, whereas the divergence regions remain almost unchanged.

Note that a great overprediction of the whirl flutter region is given by the 2D model when a low-aspect ratio blade prop-rotor is examined. The significant difference between 2D and BEM results for λ = 5·0 could be explained by the fact that for low-aspect-ratio blades 3D effects become predominant.

Finally, the stability boundaries have been predicted using also a 3D BEM frequency-domain solver based on a deformed wake shape, obtained through a free-wake analysis of the prop-rotor steady-state trim configuration. For the three-bladed prop-rotor they are depicted in Figs 18 and 19 for high-advance ratio and low-advance ratio motion, respectively.

These figures show that the effect of the wake shape adopted in the BEM analysis is not so relevant although the area of the unstable regions are underpredicted when a simple helicoidal wake is used.

5.0 CONCLUSIONS

The influence of the aerodynamic modelling on the aeroelastic analysis of prop-rotor/pylon systems has been examined. Emphasis has been given to those prediction tools that are suitable for preliminary design and control-law synthesis purposes. Specifically, 2D quasi-steady, 2D unsteady and 3D unsteady aerodynamic models have been applied to predict whirl flutter boundaries for two-bladed and three-bladed configurations, at different advance ratios and blade aspect ratios. Reduced-order modelling has been applied when unsteady aerodynamic solutions have been considered.

https://doi.org/10.1017/S0001924000002207 Published online by Cambridge University Press

The numerical investigation has shown that an increase of advance ratio has a destabilising effect on whirl flutter, whereas the increase of blade aspect ratio reduces the possibility of instability. The use of simpler aerodynamic models does not always guarantee a conservative whirl flutter analysis. This is especially true in the case of three-bladed rotors at high advance ratios, where the use of 2D aerodynamic models yields a significant underprediction of the instability regions. However, differences in the prediction of the instability regions obtained from 2D and 3D aerodynamic models appear also for two-bladed rotors at high advance ratios. Concerning the aeroelastic analyses based on the 3D BEM solver, it has been observed an appreciable effect of the wake shape used in the simulation; in particular, the whirl flutter boundaries predicted using a simple helicoidal wake shape are underpredicted with respect to those given by a distorted wake obtained from a free-wake algorithm.

REFERENCES

1. REED, W.H. and BLAND, S.R. An analytical treatment of aircraft propeller procession instability, 1961, NASA TN D-659.
2. HOUBOLT, J.C. and REED, W.H. Propeller-nacelle whirl flutter, *J Aerospace Sci*, 1962, **29**, (3), pp 333-346.
3. REED, W.H. Propeller-rotor whirl flutter: a state-of-the-art review, *J Sound and Vibration*, 1966, **4**, (3), pp 526-544.
4. SINGH, B. and CHOPRA, I. Whirl flutter stability of two-bladed proprotor/pylon systems in high speed flight, *J American Helicopter Soc*, 2003, **48**, (2), pp 99-107.
5. HATHAWAY, E.L. and GANDHI, F.S. Modeling refinements in simple tiltrotor whirl flutter analyses, *J American Helicopter Soc*, 2003, **48**, (3), pp 186-198.
6. KUNZ, D.L. Analysis of proprotor whirl flutter: Review and Update, *J Aircr*, 2005, **42**, (1), pp 172-178.
7. GENNARETTI, M. and GRECO, L. A time-dependent coefficient reduced-order model for unsteady aerodynamics of proprotors, *J Aircr*, 2005, **42**, (1), pp 138-147.
8. PETERS, D.A., KARUNAMOORTHY, S. and CAO, W. Finite state induced flow models Part I: two dimensional thin airfoil, *J Aircr*, 1995, **32**, (2), pp 313-322.
9. PETERS, D.A. and HE, C.J. Finite state induced flow models Part II: three dimensional rotor disk, *J Aircr*, 1995, **32**, (2), pp 323-333.
10. THEODORSEN, T. General theory of aerodynamic instability and the mechanism of flutter, NACA Report 496, 1935.
11. MORINO, L. and GENNARETTI, M. Boundary integral equation methods for aerodynamics, *Computational nonlinear mechanics in aerospace engineering*, ATLURI, S.N. (Ed), Aeronautics & Astronautics AIAA Series, 1992, **146**, pp 279-320.
12. JOHNSON, W. Dynamics of tilting proprotor aircraft in cruise flight, 1974, NASA TN D-7677.
13. JOHNSON, W. *Helicopter Theory*, 1980, Dover Publications, New York.
14. LOEWY, R.G. A two-dimensional approximation of unsteady aerodynamics of rotary wings, *J Aeronautical Sci*, 1957, **24**, (2), pp 81-93.

https://doi.org/10.1017/S0001924000002207 Published online by Cambridge University Press